


Article

Test on Shear Behavior of Double-Sided Thin Steel Plate Shear Wall Filled with Rigid Polyurethane Foam

Renjie Liu , Leilei Guo, Muqiao Li, Guangyong Wang * and Hang Zhao

School of Civil Engineering, Yantai University, Yantai 264005, China

* Correspondence: wanggy0609@163.com

Abstract: A double-sided thin steel plate shear wall filled with rigid polyurethane foam (SWR) is proposed. A quasi-static monotonic loading test and quasi-static cycling loading test on shear behavior and the energy dissipation capacity of the SWR were carried out. Four kinds of test specimens, including the pure steel frames, the steel frame with double-sided thin steel plates, the SWR, and the SWR with an open hole, were tested. The results showed that compared with the pure steel frame, the erection of thin steel plates on both sides enhances the shear bearing capacity, initial shear stiffness, and energy consumption capacity. It turns out that the rigid foam polyurethane (RPUF) significantly increases the shear performance of the thin steel plate shear wall. The main reason for this is that the bond effect and support effect of the RPUF delay the out-of-plane buckling of thin steel plates and improve shear performance and energy dissipation capacity.

Keywords: steel plate shear walls; seismic performance; shear performance; cycling loading; quasi-static monotonic loading energy dissipation capacity; rigid foam polyurethane



Citation: Liu, R.; Guo, L.; Li, M.; Wang, G.; Zhao, H. Test on Shear Behavior of Double-Sided Thin Steel Plate Shear Wall Filled with Rigid Polyurethane Foam. *Buildings* **2023**, *13*, 757. <https://doi.org/10.3390/buildings13030757>

Academic Editor: Francisco López Almansa

Received: 12 February 2023

Revised: 4 March 2023

Accepted: 10 March 2023

Published: 14 March 2023



Copyright: © 2023 by the authors. Licensee MDPI, Basel, Switzerland. This article is an open access article distributed under the terms and conditions of the Creative Commons Attribution (CC BY) license (<https://creativecommons.org/licenses/by/4.0/>).

1. Introduction

Steel plate shear wall (SPSW) structures, which are usually composed of embedded steel plates and edge frames, are a lateral force-resisting structural system developed in the 1970s. Steel plate shear wall structures have good plasticity, deformation ability, and stable hysteretic behavior so that they are good anti-seismic energy dissipation components and widely used in building engineering.

Research on the mechanical properties of SPSWs has been conducted, obtaining useful findings. Caccese et al. [1] studied the behaviors of unstiffened SPSWs in resisting lateral forces due to earthquake or wind based on the cycle test of six scaled specimens. They found that the thinner plate exhibited an inelastic behavior, which was mainly controlled by the yield of the thin plate, while the nonlinear system behavior was mainly due to the stretching of the plate and the formation of the diagonal tension field. Samples with thicker plates exhibited inelastic behavior that was mainly dominated by the column, and the capacity of samples with the thickest plates was limited by the instability of the column. Bhowmick et al. [2] investigated the seismic characteristics of SPSWs with eight different perforation modes using FE software. Sabouri-Ghomi and Robert et al. [3–5] and Rezia et al. [6] investigated the dynamic response of SPSWs. Berman et al. [7] focused on the shear behaviors of light-gauge SPSWs.

Various SPSWs, including stainless SPSWs, corrugated SPSWs, thin flat SPSWs, and stiffened SPSWs, have been created and their mechanical behaviors have been studied. The seismic characteristics of stainless SPSWs were investigated under low cyclic loadings [8,9]. Emami et al. [10] made a comparison between the corrugated SPSW and the thin flat SPSWs in terms of cyclic behaviors based on experimental research. Emami and Mofid [11] confirmed the effectiveness of corrugated plates in improving these behaviors. Roudsari and Farzampour et al. [12–14] analyzed the influence of opening characteristics and plate steel thickness on the shear wall performance of sinusoidal and trapezoidal corrugated

steel plates, and found that increasing the thickness of corrugated steel plates increased the bearing capacity, while square perforation reduced the bearing capacity of the shear wall more than round perforation. Wang et al. [15] studied the seismic characteristics of SPSWs with construction materials and details, and proposed a numerical method for predicting structural performance. They concluded that in high-intensity earthquake areas, load-carrying capacity, hysteretic behavior, damage modes, seismic ductility, and economic performance should be considered when choosing the appropriate form of SPSW. Mojtaba et al. [16] investigated the damage assessment method of stiffened SPSWs with different configurations under far-fault and near-fault ground motions. It was found that the configurations of SPSWs, including the distribution of openings and stiffeners, had an obvious effect on the amount of damage caused by earthquake excitations. Yang et al. [17] investigated SPSWs under shear-pressure interaction and found that the shear resistance of the SPSW decreased with an increase in the vertical load, and the failure mode of the specimen under the vertical load was due to buckling outside the plane.

Rigid polyurethane foam (RPUF) has good adhesion ability, and appreciable tensile strength, compressive strength, and shear strength [18]. In addition to good thermal insulation, it can also limit the buckling outside the plane of the thin steel plate in the SPSWs [19]. Xu et al. [20] studied the seismic performance of corrugated steel plate polyurethane composite shear wall, and analyzed the influence of main design parameters such as axial pressure ratio, steel plate height-width ratio, wall thickness, steel plate thickness, and the column flexibility coefficient on the ability of the structure to resist earthquakes. A double-sided thin steel flat plate shear wall filled with RPUF (SWR) has recently been proposed. However, the contribution of RPUF on shear performance, including the shear bearing capacity, initial shear stiffness, energy consumption ability, and equivalent viscous damping coefficient, has not been fully studied. In this paper, a test on the shear resistance and energy consumption capacity of the SWR was conducted. The failure modes, co-working mechanisms among different parts, shear bearing capacity, initial shear stiffness, energy consumption ability, and equivalent viscous damping coefficient are subsequently discussed according to the experimental phenomena and test results.

2. Test Overview

2.1. Specimens

Four specimens were tested by quasi-static monotonic loading test and another four were subjected to quasi-static cycling loading test. Figure 1 shows that the height of all specimens was 2100 mm, the width 1500 mm, and the aspect ratio of the specimens 7:5. The components included the steel frames, the thin steel plates, the foam-in-place RPUF, connecting plates, self-tapping screws, and pull-out connectors. Beams and columns were made of square tubes with Q235B steel and welded together. The cross sections of the beams and columns are shown in Figure 1. The RPUF density was 40 kg/m^3 . The RPUF fills in the cavity formed by the steel frame and the double-side thin steel plates and bonds the surrounding components. The steel plate of 0.5 mm in thickness was connected to the steel frame by self-tapping screws. The self-tapping screws spacing was 150 mm, using flat head dovetail self-tapping ST4.8 \times 25 of A3 steel. The connecting steel plate was 16 mm in thickness and made of Q235B steel. The connecting steel plate was welded together with the bottom beam of the steel frame, and connected with the bottom loading beam by bolts. Pull-out connectors were used for enhancing the corners of the walls.

The compositions of the eight samples are listed in Table 1. Two samples of one kind are the same: the one for the quasi-static monotonic loading test, and the other for the quasi-static cycling loading test. The samples for monotonic loading are numbered QT-D1, QT-D2, QT-D3, and QT-D9. Those for cycling loading are numbered QT-Z1, QT-Z2, QT-Z3, and QT-Z9. QT-D1 and QT-Z1 are pure steel frames as the control group. QT-D2 and QT-Z2 are composed of steel frames with two pairs of double-sided thin steel plates. QT-D3 and QT-Z3 were filled with the RPUF to study the effect of the RPUF on shear

resistance. The right pair of thin steel plates and RPUF in the right cavity were absent in QT-D9 and QT-Z9, to produce the effect of an opening hole on shear resistance.

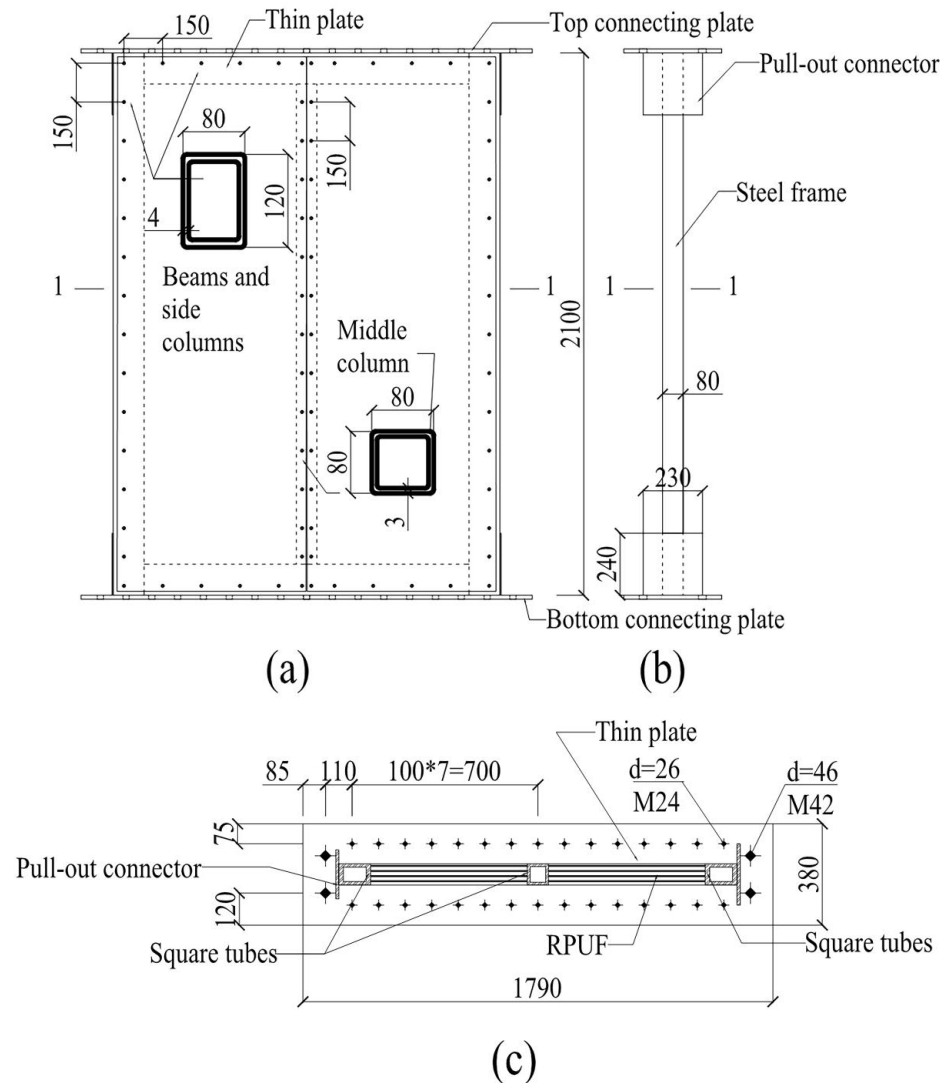


Figure 1. Schematic diagram of the specimen: (a) front view, (b) side view, (c) 1–1 section view.

Table 1. Compositions of the specimens.

Components Numbers	Steel Frame	Steel Plates	RPUF	Open Hole
QT-D1/QT-Z1	✓	×	×	×
QT-D2/QT-Z2	✓	✓	×	×
QT-D3/QT-Z3	✓	✓	✓	×
QT-D9/QT-Z9	✓	✓	✓	✓

2.2. Loading Device

The MTS electro-hydraulic servo program-controlled structural testing machine system was used for the loading. The maximum loading force of the vertical actuator was 100 kN, and the maximum loading force of the horizontal actuator was 500 kN. The brake stroke of the horizontal actuator was ± 200 mm in acting distance. To ensure the safety of the test, two compression beams were used for fixing the bottom loading beam on the ground, as shown in Figure 2.

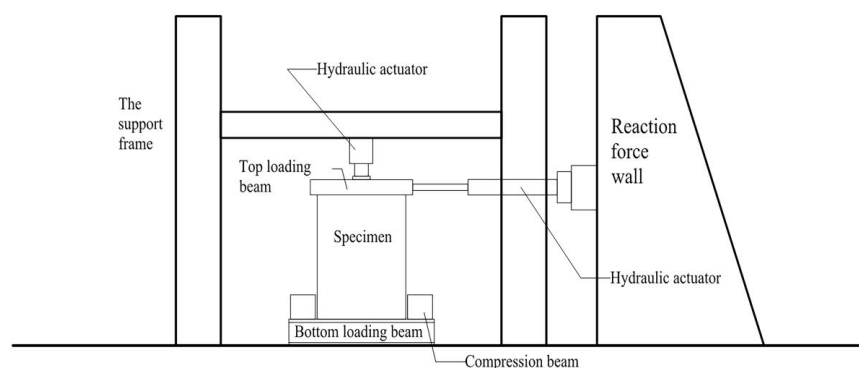


Figure 2. The loading system.

2.3. Measurement Scheme

Following JGJ 227-2011 [21], seven displacement instruments were arranged for both the monotonous horizontal loading and the low cycle reciprocating test, as shown in Figure 3. The displacement recorded by the following displacement meters is based on the ground as a reference. D1 is the horizontal displacement of the left side of the middle of the top loading beam. D2 is the horizontal displacement of the top of the wall. D3 is the lateral displacement in the middle of the wall. D4 is the horizontal displacement at the bottom of the wall. D5 and D6 are the vertical displacement on both sides of the wall. D7 is the horizontal displacement of the bottom loading beam.

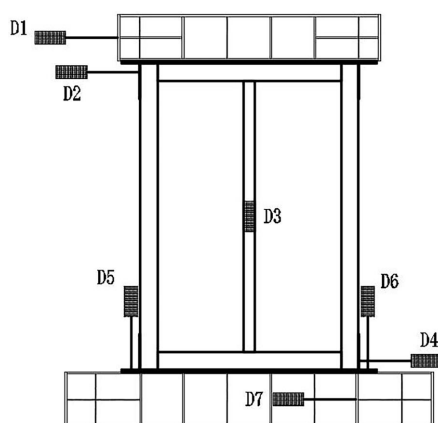


Figure 3. Displacement measuring points.

2.4. Loading Plan

The loading plans of the quasi-static monotonic loading and the quasi-static cycling loading were designed according to JGJ T101-2015 [22].

2.4.1. Quasi-Static Monotonic Loading

The vertical load was first applied by 40 kN and remained constant during loading. The horizontal loading was applied with load control mode in the early stage, and the horizontal load was applied grade by grade with a difference of 10 kN. The load control mode was transferred to displacement control mode after obvious yield of the specimens. Then, the load was applied grade by grade with a difference of 10 mm until the specimens were damaged or the hydraulic actuator reached the maximum range. After each grade of the load was completed, the load was kept for 2 min, and the results were collected after the deformation of the specimens were stable.

2.4.2. Quasi-Static Cycling Loading

The vertical load was treated in the same way as the monotonic loading. The horizontal loading plan for the quasi-static cycling loading is displayed in Figure 4. First, the specimens

were subjected to five stages of single cyclic loading to the approximate yield displacement Δy was estimated by the horizontal monotonic loading test results. Then, the displacement control mode was continued for the following stages, and incremented at $0.5 \Delta y$ for each loading grade until the specimens were damaged. There were three cycles repeated in each stage. During cyclic loading, test data were collected continuously in real time.

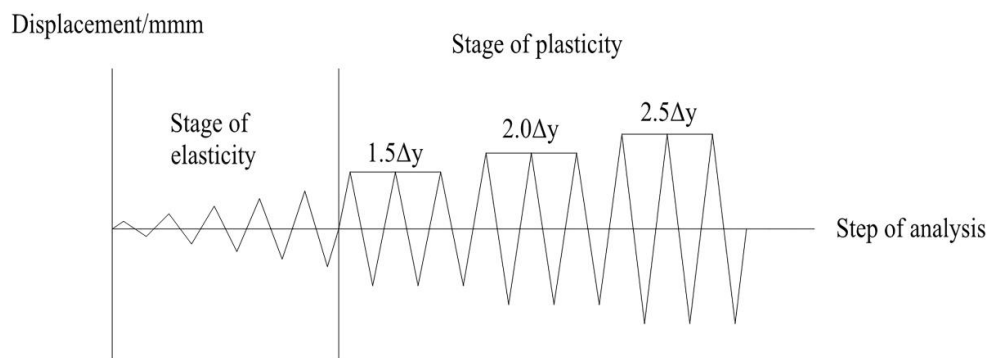


Figure 4. Plan of the quasi-static cycling loading.

3. Test Phenomena

3.1. Quasi-Static Monotonic Loading

Throughout the loading process on QT-D1, there was no other phenomenon except steel frame deformation. Figure 5 shows that when the horizontal relative displacement of the top loading beam was 64 mm, the horizontal force reached the peak value of 70.1 kN and then very slowly decreased. This indicates that QT-D1 had good ductility. Figure 6 shows that when the horizontal displacement of the loading beam reached 144 mm, the side column depressed obviously beside the edges of the pull-out connecting plates; then, the loading stopped.

During the first stage loading on QT-D2, the specimen made a clear sound and the thin steel plates appeared slightly wrinkled. The sound was due to the out-of-plane buckling of the thin steel plates. Because the cavity between the double-sided thin steel plates was empty, the thin steel plates lacked out-of-plane support. The thin steel plates kept making sounds during loading and the wrinkled region on the thin steel plates kept growing. When the loading reached 78 kN, an apparent sound appeared and the load-displacement curve showed obvious twist and downturn, as shown in Figure 5. This was due to the out-of-plane buckling developing seriously and suddenly of the thin steel plates. When the horizontal displacement of the top loading beam was 36 mm, the thin steel plates began tearing from the regions near the screws on the middle column. After that, the load value remained basically unchanged, but the thin steel plates kept tearing. When the horizontal displacement was 51 mm, the shear bearing capacity was no longer increased and reached the peak value of 84.9 kN. When the horizontal relative displacement reached 71 mm, the bottom part of the left thin steel plates and the top part of the right thin steel plates were completely torn and destroyed by screws, as shown in Figure 7. When the horizontal displacement of the loading beam reached 141 mm, the loading stopped. Compared with QT-D1, the shear strength and the initial shear stiffness of QT-D2 increased by up to 21% and 142%, respectively.

During the first stage loading on QT-D3, the wall specimen deformed linearly. A slight muffled sound occurred and kept going until the load reached 30 kN, but no wrinkle was observed. The slight muffled sound indicated that the thin steel plates were partially detached from the RPUF. When the force reached 40 kN, a small bulge appeared at the corners of the thin steel plates. This bulge kept growing as the sound continued. When the loading force reached 60 kN at the sixth stage, a large noise was heard, indicating a significant turning point on the load-displacement curve, as shown in Figure 5. When the loading force was 90 kN, at the top part of the right thin steel plates appeared a large oblique bulge; the load-displacement curve suddenly dropped, and then the displacement

control began. When the horizontal displacement was 31 mm, the sound became constant, and the bulge kept increasing. The thin steel plates kept detaching from the RPUF. When the displacement reached 41 mm, the thin steel plates started tearing from the screws near the middle column. The tearing of the thin steel plates in QT-D1 was significantly later than in QT-D2. When the displacement reached 51 mm, the bulge in the bottom left corner of the left panel and the bottom left corner of the right panel suddenly worsened, and the force reached its peak value of 101.6 kN. When the displacement was 101 mm, the bottom right corner of the right thin steel plates was seriously torn, and the thin steel plates tore at the middle column. When the horizontal displacement reached 131 mm, a large area of the top part of the left panel suddenly broke away from the RPUF, as shown in Figure 8. When the horizontal displacement reached 141 mm, a crisp sound was heard and the loading process ended. The sound was due to the fracture of the ends of the middle column in the steel frame.

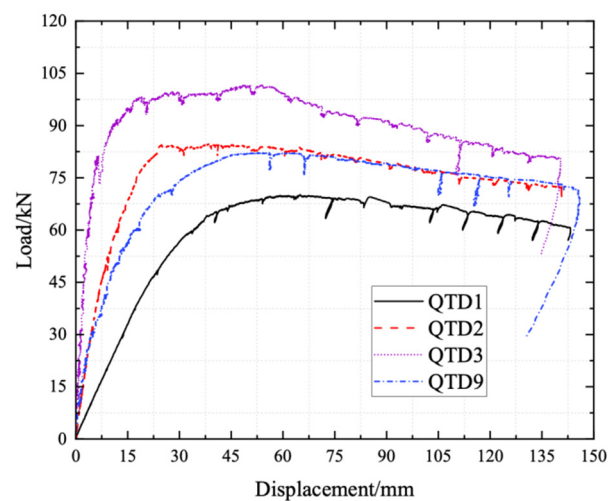


Figure 5. Load-displacement curves under the horizontal monotonic loading.



Figure 6. Failure image of QT-D1.



Figure 7. Failure image of QT-D2.



Figure 8. Failure image of QT-D3.

Compared with QT-D1, the shear bearing capacity and the initial shear stiffness of QT-D3 increased by up to 45% and 233%, respectively. Compared with QT-D2, those of QT-D3 increased by up to 20% and 38%, respectively. It turns out that the RPUF significantly increases the shear bearing capacity and the initial shear stiffness of the SWR. However, the RPUF was seriously damaged, as shown in Figure 8. This indicates that the strength of the RPUF was low. The main reason for this is that the RPUF bonds components together, prevents the out-of-plane buckling of thin steel plates, and enhances the integrity of the SWR.

During the first loading stage on QT-D9, the specimen deformed linearly. A slight muffled sound occurred and kept going until the load reached 30 kN. In the third stage, the bottom right corner of the right thin steel plates made a sound and a slight fold appeared. Similar to QT-D3, the slight muffled sounds continued during loading. When the horizontal displacement reached 55 mm, it was observed that the horizontal force reached its peak value of 82.1 kN, as shown in Figure 5. In the tenth loading stage, when the displacement control reached 65 mm, the thin steel plates tore near the screws on both sides of the wall, as shown in Figure 9. Compared with QT-D1, the shear bearing capacity and the initial shear stiffness of QT-D9 increased by up to 19% and 141%, respectively. This also showed that the shear bearing capacity and the initial stiffness of QT-D2 and QT-D9 were almost the same, and load-displacement curves of the two specimens were very close, as shown in Figure 5. This indicates that the contribution of the RPUF on the shear bearing capacity and the initial stiffness could be approximately equal to that of two 0.5 mm steel plates.

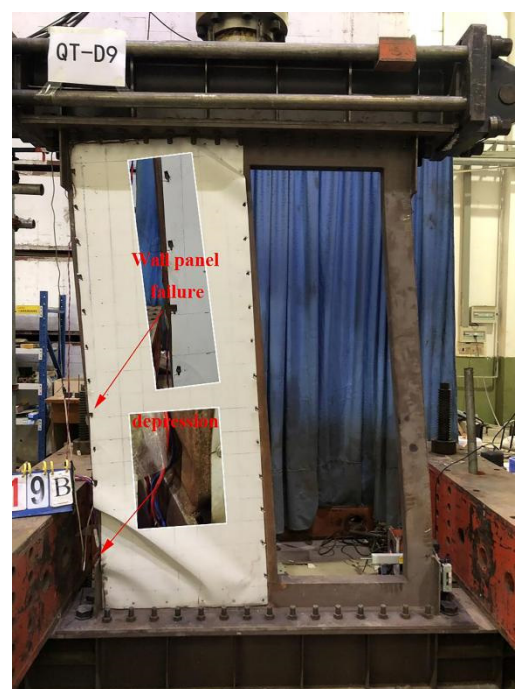


Figure 9. Failure image of QT-D9.

3.2. Quasi-Static Cycling Loading

When the horizontal displacement was 60 mm in QT-Z1, sound from the steel frame could be heard, and cracks were observed at the top and the bottom roots of the column in the steel frame, as shown in Figure 10. When the horizontal displacement was 75 mm, the edge area of the lateral pull-out connecting plates of the bottom side columns sagged. With the increase of horizontal displacement, the concave and the convex ranges of both sides of the side columns near the edge of the pull-out connecting plates gradually expanded. When the horizontal displacement was pushed to 90 mm for the second time, a slight sound appeared again, the root of the middle column was seriously fractured, and the frame of the pull-out connecting plates of the side column completely cracked, as shown in Figure 10. This was regarded as the eventual damage and the loading was terminated. In QT-Z1, the serious cracks on the steel frame led to the eventual failure.

Sound from the thin steel plates appeared at the first stage of loading on QT-Z2 and increased as the horizontal displacement increased. At the sixth stage of the loading process, the seam of the thin steel plates was torn by screws, the left and right sides of the thin steel plates damaged by screws, and the thin steel plates bulged considerably. When the horizontal displacement reached 40 mm at the seventh stage, a depression appeared at the edge of the pull-out connecting plate in the bottom right corner of the steel frame; the

thin steel plates were seriously damaged and lost shear bearing capacity. At the 12th stage, when the horizontal displacement was pushed to 70 mm, the left column was seriously dented and the top part of the thin steel plates fell off, as shown in Figure 11. The loading was then ended. This shows that the failure mode of QT-Z2 was that the thin steel plates lost shear capacity at an early stage due to tearing near the screws and the serious cracks on the steel frame led to the eventual failure.

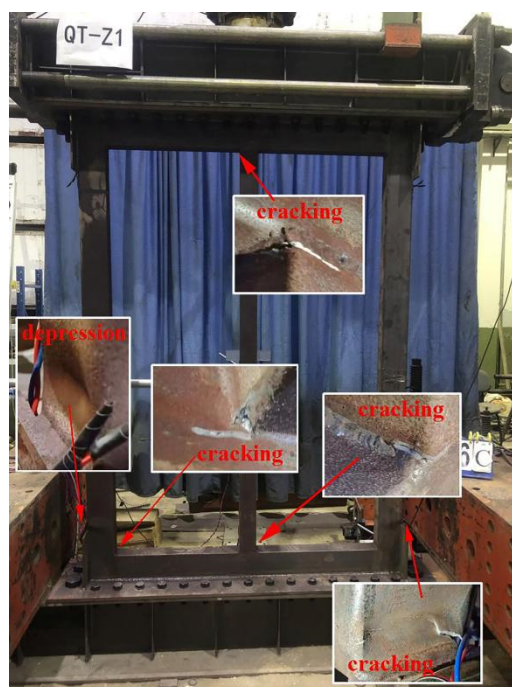


Figure 10. Failure image of QT-Z1.

During the first stage of the loading process on QT-Z3 there appeared both an oblique bulge whose length increased and a muffled noise. When the displacement was 2 mm, a slight bulge was observed on the right wall panel. In the second stage, a drum song occurred in the upper right corner of the left wall panel. During the third stage, the bulge area of the left wall panel became larger, and appeared in the bottom left corner of the right wall panel. During the fourth stage, the left wall panel bulge was run through diagonally, and the sound was louder. When the displacement was pulled to 8 mm, the bulge of the right wall panel was run through diagonally as well. In the sixth state, a bulge occurred in the upper right corner of the left wall panel, and a large bulge in the bottom right corner of the right wall panel appeared with continuous sound. The wall panel continued to detach from the RPUF, and the thin steel plates near the middle of the wall were torn by screws. In the tenth stage, the thin steel plates were indented near most screws in the middle column, and most of the edge of the wall panel slipped. At the 19th stage, when the horizontal displacement reached 85 mm, a large crack appeared in the bottom right column of the steel frame, as shown in Figure 12, which was regarded as the failure of the wall. Compared with the failure image of QT-Z2, most of the area of the thin steel plates in QT-Z3 maintained a neat and flat appearance, with only a small region on the top and bottom parts bulged. This difference was due to the contribution of the RPUF by the bond and the support function, so that thin steel plates possessed better shear resistance.



Figure 11. Failure image of QT-Z2.



Figure 12. Failure image of QT-Z3.

When the displacement of QT-Z9 reached 10 mm, a slight bulge and fold were observed at the bottom left corner of the left wall panel. During the third stage, the middle part of the wall panel bulged and the sound continued. When the displacement reached 40 mm, the thin steel plates were torn near the screws. In the ninth stage, the back wall panel buckled and the folds increased. Most of the screws were indented, and most of the edge of the wall panel slipped. In 16th stage, when the displacement reached 85 mm, large cracks appeared at the bottom of the middle column, as shown in Figure 13, and loading stopped. The damage mode was the same as QT-Z3.

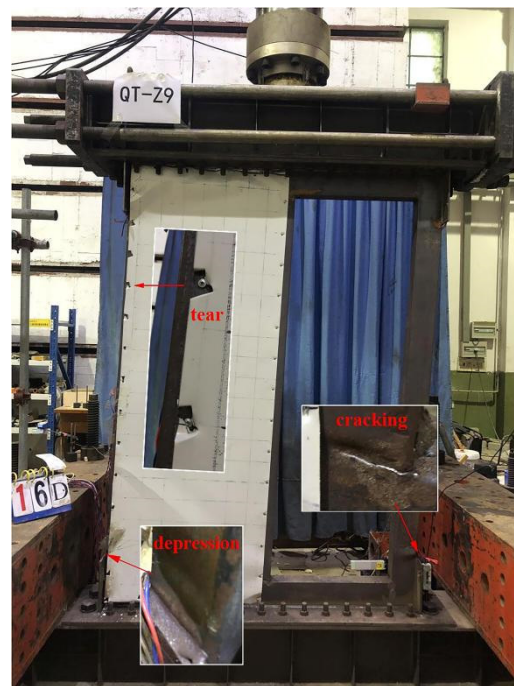


Figure 13. Failure image of QT-Z9.

4. Test Results

4.1. Load-Lateral Hysteretic Curves

Figure 14 shows that the hysteresis loops of QT-Z1 was full and spindle. This shows that the ductility and energy dissipation capacity was good. As shown in Figures 15–17, QT-Z2, QT-Z3, and QT-Z9 show a pinch phenomenon in the first five cycles, but full and spindle cycles during the later stages. This is because the thin steel plates and the RPUF work together with the steel frame in the early stages. After however, the thin steel plates and the RPUF fail and the steel frame bears most of the load. We conclude that the mechanism works as follows. At the early loading stage, the steel frame, thin steel plates, and the RPUF work together. Then, due to the buckling of the steel plates, the stiffness of the specimen decreases gradually. When the direction of loading turns, thin steel plates enter in the recovery process, and the steel frame bears most of the horizontal load. When the thin steel plates are in the deformation state, the three work together again. In the late stages, the thin steel plates are damaged, and the steel frame and the RPUF work together. In the end, the steel frame gradually yields, the RPUF is damaged, and the stiffness decreases.

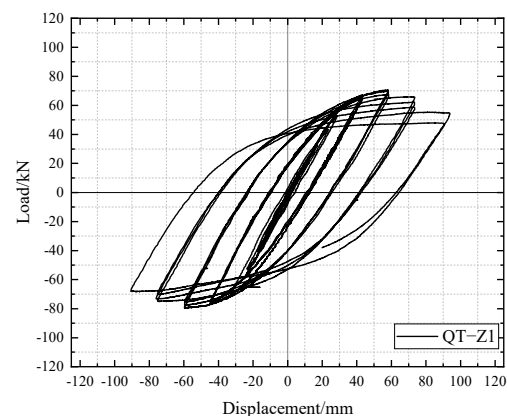


Figure 14. Load-lateral hysteresis curve of QT-Z1.

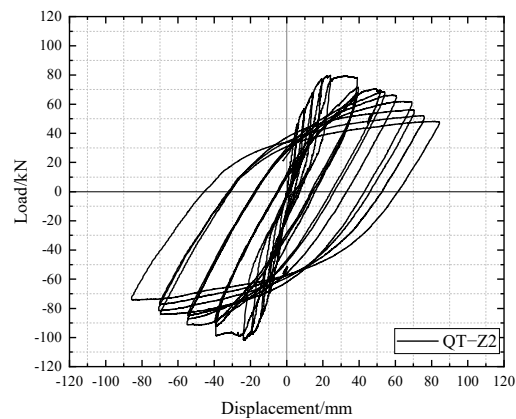


Figure 15. Load-lateral hysteresis curve of QT-Z2.

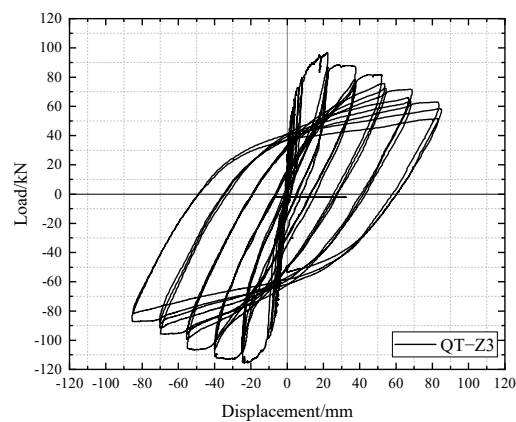


Figure 16. Load-lateral hysteresis curve of QT-Z3.

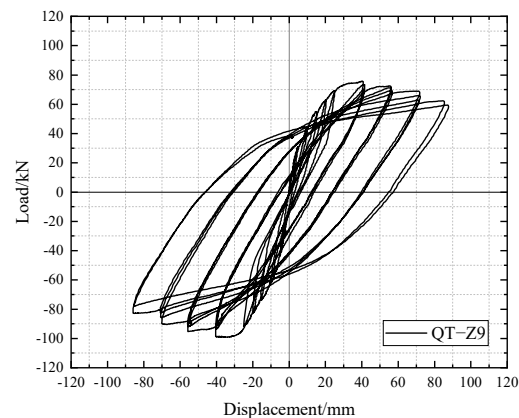


Figure 17. Load-lateral hysteresis curve of QT-Z9.

QT-Z1 and QT-Z2 show that, with the use of steel plates, a pinch effect appears in the hysteresis curve of the specimen, the peak load is larger, the initial loading stiffness is higher, and the hysteresis curve is fuller. This is because the thin steel plates and the steel frame are connected by screws. Thus, they share the horizontal load at the early stage. For QT-Z2 and QT-Z3, the pinching effect in the early stage of both specimens gradually increases and the peak value of load increases. This is because the RPUF can effectively cooperate with the thin steel plates to bear the horizontal load, constrain the bulging deformation of the thin steel plates, and improve the bearing capacity and stiffness of the specimens. Compared with QT-Z2 and QT-Z9, QT-Z3 has the highest peak load and the fullest hysteretic curve. There is a small difference between QT-Z9 and QT-Z2 in the load peak, and the pinching effect of QT-Z9 is more obvious than that of QT-Z2. This

is because, as the RPUF fills in the space between the thin plates, the stiffness of the plates increases.

4.2. Skeleton Curves

Figure 18 shows the skeleton curves of the four specimens. Compared with the other specimens, QT-Z1 reached the peak value with the largest displacement. This indicates that the stiffness was lower. This is because it had no thin steel plate or RPUF. Compared with QT-Z1, the shear bearing capacity of QT-Z2, QT-Z3, and QT-Z9 increased by 27.79%, 44.74%, and 19.21%, respectively. We concluded that thin steel plates and RPUF can effectively improve the shear bearing capacity of the specimens. QT-Z2 and QT-Z3 had the same decline rate and yield severity after the load reached the maximum value. These were greater than the decline rate and yield severity of QT-Z1 and QT-Z9. This shows that the stiffness and shear bearing capacity is significantly reduced after the thin steel plates and the RPUF fail. The shear bearing capacity of the steel frame does not significantly decrease after reaching the peak, and the yield only appears locally. The steel frame still bears the horizontal load, and the bearing capacity decreases sharply until the connection between the frame columns and the frame beams is damaged. When all the specimens reached their ultimate failure states, the lateral displacement was within 90 mm, and the inter-story displacement angle did not reach 1/50, which is up to code [23].

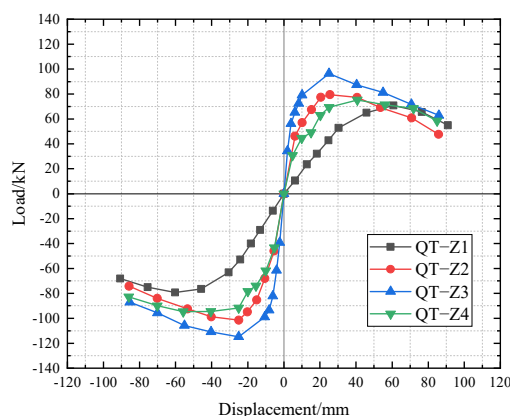


Figure 18. Skeleton curves.

4.3. Stiffness Degradation Curves

The stiffness of the specimen decreases with the increase of the number of load cycles and displacement. Following regulation [21], stiffness degradation curves are used to represent the stiffness at different times. Figure 19 shows that the stiffness degradation curves of all the samples were smooth. Since QT-Z1 had no thin steel plates or RPUF, stiffness in the early stages is low, and the stiffness degradation rate is slow. The initial stiffness of QT-Z3 is the largest, eight times that of QT-Z1. However, the stiffness degradation rate of QT-Z1 is the fastest in the early stages, due to the failure of the thin steel plates and RPUF. The stiffness degradation curves of QT-Z2 and QT-Z9 are not much different, and the initial stiffness is four times that of QT-Z1. The stiffness degradation rate of QT-Z2 and QT-Z9 is very fast at the early stages, but as the loading displacement increases, the stiffness degradation rate decreases significantly, remaining basically unchanged at the late stages. At the end of loading, all the curves tended to horizontality. This is because only the steel frame works at the end of the loading stages.

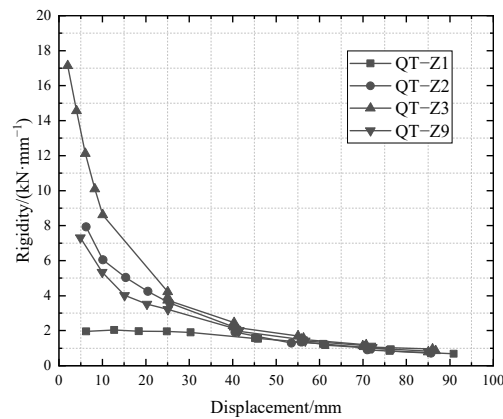


Figure 19. Stiffness degradation curves.

4.4. Bearing Capacity Degradation

The bearing capacity degradation coefficient is a measure of the degree to which the bearing capacity of the specimen decreases with the number of loading cycles. Figures 20 and 21 show the degradation coefficients λ_2 and λ_3 of all the specimens, respectively. λ_2 and λ_3 respectively represent the peak load of the second and third cycles and the previous peak load in the same displacement loading stage. In addition to λ_2 of QT-Z1 being 1.026 times greater than 1, the degradation coefficients of the other specimens are less than 1. Most of the distribution being in 0.90~1.0, the curve basically shows a decreasing trend with the increase of displacement. The bearing capacity degradation coefficients λ_3 of all the specimens show similar trends as those of λ_2 . As the shear bearing capacity was stable, the specimens demonstrated good plasticity and ductility.

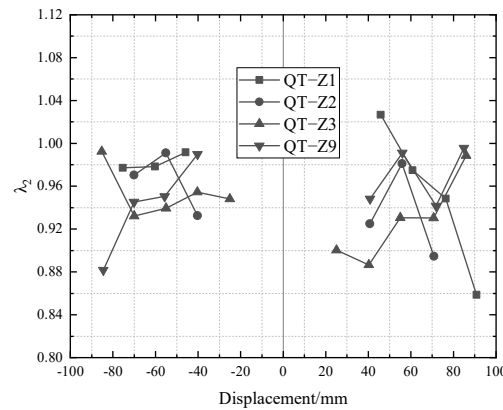


Figure 20. Degradation coefficient λ_2 .

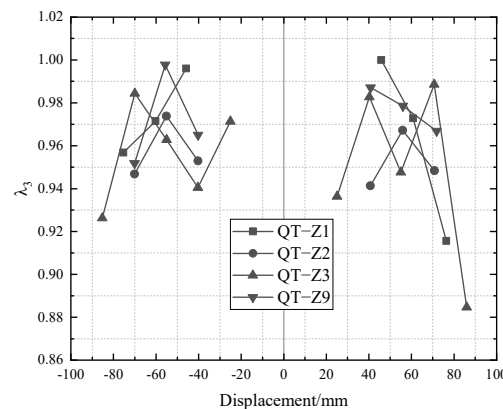


Figure 21. Degradation coefficient λ_3 .

4.5. Energy Dissipation Capacity

The area of the graph surrounded by the load-displacement hysteresis curve represents the energy consumption capacity of the sample. The fuller the hysteresis curve is, the higher the equivalent viscous damping coefficient is; the larger the area is, the greater the energy dissipation energy is. The energy consumption curves and the equivalent viscous damping coefficient curves are shown in Figures 22 and 23, respectively. Figure 22 shows that in early loading stages, the energy consumption values of QT-Z1 are the lowest, those of QT-Z3 the highest, and those of QT-Z2 and QT-Z9, in between the previous two, are almost the same. The main reason for this is that, in the early stages, the steel frame is in an elastic stage, but the thin steel plates and the RPUF yield and contribute to energy consumption. As the displacement increased, the energy consumption capacity of QT-Z1 rose the fastest, those of QT-Z2 and QT-Z9 second-fastest, and the curve of QT-Z3 the slowest, remaining basically linear. This is because the steel frame starts yielding and contributes to energy consumption. In the late stages, the energy consumption capacity of all the samples was almost the same. The reason for this is that the thin steel plates and RPUF were badly damaged and the steel frame plays the main role in energy consumption. Figure 23 shows that the changing trend of the equivalent viscous damping coefficient of QT-Z1 is consistent with the energy consumption capacity. The basic changing trend of the equivalent viscous damping coefficients of QT-Z2, QT-Z3, and QT-Z4 is in agreement with the energy consumption capacity, but more complicated in the early stages.

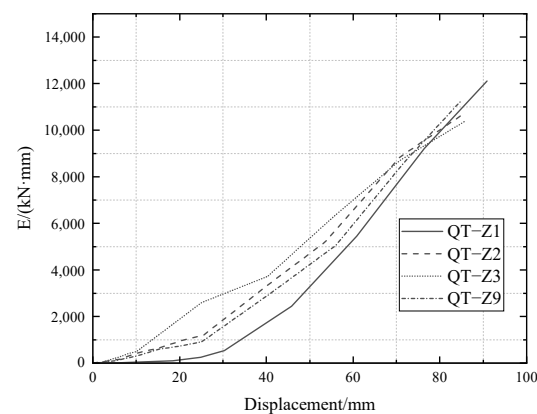


Figure 22. Energy consumption curves.

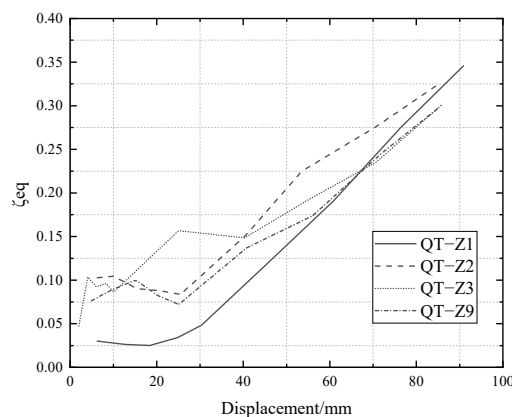


Figure 23. Equivalent viscous damping coefficient curves.

5. Conclusions

The shear performance of SPSW can be improved by being filled with RPUF. Tests were conducted on shear behaviors and the energy consumption capacity of double-sided steel plate shear wall filled with RPUF. Both the quasi-static monotonic loading test and quasi-static cycling loading test were carried out to analyze the work mechanism, shear

bearing capacity, initial shear stiffness, energy consumption capacity, and the equivalent viscous damping coefficient. The conclusions are as follows.

Compared with a steel frame, the shear resistance of the steel frame with double-sided steel plates, the SWR, and the SWR with a door hole increases by 21%, 45% and 19%, respectively. Compared with a steel frame, the initial shear stiffness of those specimens increases by 142%, 233%, and 141%, respectively. It turns out that the RPUP contributes significantly to the shear bearing capacity and the initial shear stiffness of the thin SPSW. The main reason for this is that the bond effect and support effect of the RPUP delay the out-of-plane buckling of thin steel plates.

Compared with a steel frame, the energy consumption capacity of the steel frame with double-sided steel plates, the SWR, and the SWR with a door hole increases by up to 260%, 333%, and 52%, respectively. Compared with a steel frame, the equivalent viscous damping coefficient of those samples increases by up to 298%, 333%, and 52%, respectively. We conclude that the RPUP contributes significantly to the energy consumption capacity and the equivalent viscous damping coefficient of the SWR.

There are two energy consumption modes: one is the deformation-recovery-deformation of thin steel plates, and the other is the inelastic deformation of the steel frame. In early stages, the steel frame of the SWR is in an elastic stage, but thin steel plates and the RPUP yield and contribute to energy consumption. In the late loading stage, thin steel plates and the RPUP of the SWR are badly damaged and the steel frame plays the main role in energy consumption. The thin steel plates and the RPUP cooperate well with the steel frame to bear the horizontal load, and enhance the stiffness, bearing capacity, and energy consumption capacity.

Author Contributions: Conceptualization, R.L. and M.L.; methodology, L.G.; software, M.L.; validation, H.Z.; dynamic analysis, H.Z.; investigation, L.G.; writing—original draft preparation, R.L.; writing—review and editing, G.W.; visualization, L.G.; supervision, G.W.; project administration, R.L.; funding acquisition, R.L. All authors have read and agreed to the published version of the manuscript.

Funding: This research was funded by the Natural Science Foundation of Shandong, grant number ZR201911030049.

Data Availability Statement: All data are presented in the paper. There is no additional data.

Conflicts of Interest: The authors declare no conflict of interest.

References

1. Vincent, C.; Elgaaly, M.; Chen, R.M. Experimental study of thin steel-plate shear walls under cyclic load. *J. Struct. Eng-Asce.* **1993**, *119*, 573–587. [[CrossRef](#)]
2. Bhowmick, A.K.; Grondin, G.Y.; Driver, R.G. Nonlinear seismic analysis of perforated steel plate shear walls. *J. Constr. Steel Res.* **2014**, *94*, 103–113. [[CrossRef](#)]
3. Roberts, T.M.; Ghomi, S.S. Hysteretic characteristics of unstiffened perforated steel plate shear panels. *Thin Wall Struct.* **1992**, *14*, 139–151. [[CrossRef](#)]
4. Roberts, T.M.; Shahabian, F. Ultimate resistance of slender web panels to combined bending shear and patch loading. *J. Constr. Steel Res.* **2001**, *57*, 779–790. [[CrossRef](#)]
5. Ghomi, S.S.; Roberts, T.M. Nonlinear dynamic analysis of steel plate shear walls including shear and bending deformations. *Eng. Struct.* **1992**, *14*, 309–317. [[CrossRef](#)]
6. Rezai, M. Seismic Behaviour of Steel Plate Shear Walls by Shake Table Testing. Ph.D. Thesis, The University of British Columbia, Vancouver, BC, Canada, 1999. [[CrossRef](#)]
7. Berman, J.W.; Bruneau, M. Experimental Investigation of Light-Gauge Steel Plate Shear Walls. *J. Struct. Eng-Asce.* **2003**, *131*, 259–267. [[CrossRef](#)]
8. Wang, M.; Wang, W.G.; Wang, Y.Q.; Chang, T.; Shi, Y.J. Study on hysteretic constitutive model of austenitic stainless steel. *Eng. Mech.* **2015**, *32*, 107–114. [[CrossRef](#)]
9. Chang, X.; Yang, L.; Wang, M.; Yin, F. Study on constitutive model of austenitic stainless steel and duplex stainless steel under cyclic loading. *Eng. Mech.* **2019**, *36*, 137–147. [[CrossRef](#)]
10. Emami, F.; Mofid, M.; Vafai, A. Experimental study on cyclic behavior of trapezoidally corrugated steel shear walls. *Eng. Struct.* **2013**, *48*, 750–762. [[CrossRef](#)]

11. Emami, F.; Mofid, M. On the hysteresis behavior of trapezoidally corrugated steel shear walls. *Struct. Design Tall Spec. Build.* **2014**, *23*, 94–104. [[CrossRef](#)]
12. Roudsari, S.S.; Soleimani, S.M.; Hamoush, A.S. Analytical study of the effects of opening characteristics and plate thickness on the performance of sinusoidal and trapezoidal corrugated steel plate shear walls. *J. Constr. Steel Res.* **2021**, *182*, 106660. [[CrossRef](#)]
13. Farzampour, A.; Laman, J.A.; Mofid, M. Behavior prediction of corrugated steel plate shear walls with openings. *J. Constr. Steel Res.* **2015**, *114*, 258–268. [[CrossRef](#)]
14. Farzampour, A.; Mansouri, I.; Hu, J.W. Seismic Behavior Investigation of the Corrugated Steel Shear Walls Considering Variations of Corrugation Geometrical Characteristics. *Int. J. Steel Struct.* **2018**, *18*, 1297–1305. [[CrossRef](#)]
15. Wang, M.; Yang, W.G.; Shi, Y.J.; Xu, J. Seismic behaviors of steel plate shear wall structures with construction details and materials. *J. Constr. Steel Res.* **2015**, *107*, 194–210. [[CrossRef](#)]
16. Labibzadeh, M.; Khayat, M. Damage assessment of stiffened steel plate shear walls with different configurations under far-fault and near-fault ground motions. *J. Constr. Steel Res.* **2023**, *200*, 107685. [[CrossRef](#)]
17. Lv, Y.; Li, L.; Wu, D.; Zhong, B.; Chen, Y.; Chouw, N. Experimental Investigation of Steel Plate Shear Walls under Shear-Compression Interaction. *Shock. Vib.* **2019**, *2019*, 8202780. [[CrossRef](#)]
18. Stirna, U.; Beverte, I.; Yakushin, V.; Cabulis, U. Mechanical properties of rigid polyurethane foams at room and cryogenic temperatures. *J. Cell. Plast.* **2011**, *47*, 355–377. [[CrossRef](#)]
19. Wu, Y.W.; Fan, S.G.; Zhou, H.; Wu, Q.X. Cyclic behaviour of diagonally stiffened stainless steel plate shear walls with two-side connections: Experiment, simulation and design. *Eng. Struct.* **2022**, *268*, 114756. [[CrossRef](#)]
20. Xu, Q.; Liu, H.W.; Qiao, W.T.; Wang, C.H. Finite element analysis on seismic behavior of a new prefabricated corrugated steel plate and polyurethane composite shear wall. *Steel Constr.* **2021**, *36*, 1–8. [[CrossRef](#)]
21. *JGJ227-2011*; Technical Specification for Low-Rise Cold-Formed Thin-Walled Steel Buildings. China Architecture & Building Press: Beijing, China, 2011.
22. *JGJ T101-2015*; Specification for Seismic Test of Buildings. China Architecture & Building Press: Beijing, China, 2015.
23. *GB50011-2010*; Code for Earthquake Design of Buildings, 2016th ed. China Architecture & Building Press: Beijing, China, 2010.

Disclaimer/Publisher’s Note: The statements, opinions and data contained in all publications are solely those of the individual author(s) and contributor(s) and not of MDPI and/or the editor(s). MDPI and/or the editor(s) disclaim responsibility for any injury to people or property resulting from any ideas, methods, instructions or products referred to in the content.